



HAL
open science

Simulation of a set of large-size thermal enclosures by a substructured reduced-order model

Benjamin Gaume, Frédéric Joly, Olivier Quemener

► To cite this version:

Benjamin Gaume, Frédéric Joly, Olivier Quemener. Simulation of a set of large-size thermal enclosures by a substructured reduced-order model. *Experimental Heat Transfer*, 2021, 50 (4), pp.3300–3324. 10.1002/htj.22029 . hal-03122649

HAL Id: hal-03122649

<https://hal.science/hal-03122649>

Submitted on 30 Jun 2024

HAL is a multi-disciplinary open access archive for the deposit and dissemination of scientific research documents, whether they are published or not. The documents may come from teaching and research institutions in France or abroad, or from public or private research centers.

L'archive ouverte pluridisciplinaire **HAL**, est destinée au dépôt et à la diffusion de documents scientifiques de niveau recherche, publiés ou non, émanant des établissements d'enseignement et de recherche français ou étrangers, des laboratoires publics ou privés.

Simulation of a set of large-size thermal enclosures by a substructured reduced-order model

Benjamin Gaume | Frédéric Joly | Olivier Quéméner

LMEE, Univ Evry, Université Paris-Saclay, Evry, France

Correspondence

B. Gaume, LMEE, Univ Evry, Université Paris-Saclay, 91020 Evry, France.
Email: b.gaume@iut.univ-evry.fr

Abstract

In the context of simulations of coupled thermal enclosures, we present here a substructuring technique adapted to the amalgam reduced-order modal model (AROMM). This technique consists of splitting the geometry into different zones. A modal model is then applied to each zone, and the coupling of the resulting models is performed via a thermal contact resistance. This technique allows the consideration of physical thermal resistances between different components of the geometry, as well as the making of fictitious cuts within a continuous domain, when its large size causes difficulties in obtaining the global reduced model. Applied to the simulation of a simplified component of a liquefied natural gas carrier, the use of a substructured model with 200 modes allows an access to the whole temperature field with a maximum difference near 1 K and an average difference of the order of 0.2 K, compared with a conventional Lagrange finite-element model of shell type, which requires 60 times longer calculation.

KEYWORDS

enclosure, finite elements, modal reduction, reduced model, substructuring, thermal contact resistance, thermal simulation

1 | INTRODUCTION

The liquefied natural gas (LNG) and its transportation by tankers play an increasingly important role in the field of energy. The LNG transportation volume is 330 billions m^3 (30% of global exported volume). Membrane technology, which is the one studied in this article, constitutes nearly 85% in terms of order book. This technology allows the design of very large ships, which can contain LNG volumes higher than 200.000 m^3 . When designing these ships, a major problem is the risk of mechanical breakage due to the extremely cold walls of the vessel, as it contains several large tanks of natural gas kept in a liquid state at -163°C . Accurate knowledge of temperature fields is then a necessity, which generates the development of specific computer codes.

This configuration corresponds to the thermal problem of enclosures, for which different kinds of studies have been carried out. Many studies focused first on the study of heat transfer by natural convection inside closed cavities. Except for some recent articles corresponding to analytical studies validated by experiences in simple configurations,¹ the studies correspond generally to numerical tools development, usually for two-dimensional (2D) geometries² and sometimes for 3D configurations.³

All of these studies include the assumption of a natural flow and require the meshing of the walls and of the gas contained in the enclosure. They are, therefore, limited to a simple configuration. Thus, for the complex geometry, the solution is to discretize only the wall. It is then considered that the internal fluid is characterized by a single temperature and that this fluid exchanges a convective flow with the walls via a convection coefficient h , which is known either from correlations or from experiences.

For the study of a set of enclosures characterized by a complex geometry, the mesh of the walls leads to a large number of unknowns. Various simplified models can be used, which generally provide the average temperatures of wall surfaces: the study reported in Reference [4] offered a simple parametric model, whose coefficients are identified for a given geometry by a complete set of numerical simulations for various stresses. The study reported in Reference [5] examined a steady-state model for a 3D configuration, taking into account the conduction and the convection effects, where each wall is characterized by a simple 1D resistance. In a similar way, studies reported in References [6,7] used the technique of RC networks to determine the wall temperatures.

To determine the complete thermal fields of the walls, a possibility is to develop plate⁸ or shell models.^{9,10} In these models, the walls are considered as a superposition of layers. One then seeks to resolve a set of coupled dimensional problems along the thickness of the wall. The study reported in Reference [11] proposed another model in which a single plate is considered, but it is characterized by three points in the direction of thickness. Finally, when we can consider that the wall is sufficiently thin and heat-conductive to consider only one temperature in the thickness, it is possible to use a simple degenerated 2D model, often proposed by industrial computer codes. The problem posed in this paper corresponds to this configuration.

However, even if a shell model is used, calculation of the temperature for the entire ship's structure requires significant CPU time, and it is incompatible with a goal of online predictions of the ship's thermal behavior in case of technical problems. The idea is to use model reduction methods based on modal formulation. The most used technique is the proper orthogonal decomposition (POD) method that requires the knowledge of thermal fields to get a reduced basis. Initiated in the field of fluid mechanics, numerous thermal studies were performed.¹²⁻¹⁴ Recently, similar methods have emerged: such as the APHR method¹⁵ and the PGD approach.¹⁶ There is another technique that is particularly suitable for inverse problems: It is the

MIM method, in which the reduced model is directly identified without computing or identifying the modal basis. The latest works^{17,18} focus on control command problems.

Finally, another approach is to solve an eigenvalue problem adapted to the thermal problem, which gives access to knowledge of a complete modal basis. In using specific techniques, the knowledge of this basis allows to obtain a reduced model. Initially, the so-called classical bases were obtained from an eigenvalue problem for which boundary conditions matched those of the thermal problem posed.^{19,20} This method was limited to thermal problems characterized by linear and stationary parameters. The generalization of this technique to all thermal problem types has subsequently been made possible by the use of the amalgam reduced-order modal model (AROMM) method,^{21,22} previously called as the BERM method.²³⁻²⁵

In parallel to this issue of rapid calculations, another difficulty is the consideration of thermal contact resistance that can affect the thermal behavior of the structure. One solution is to use the substructuring technique, in which the different substructures in an imperfect thermal contact are coupled by the heat flux. It is used in industrial computer codes using the finite-element/volume method (Comsol, Fluent). The adaptation of this substructuring technique for the various reduction methods mentioned above has already been studied (Reference [26] for the MIM, References [27,28] for the method using conventional modal bases, and Reference [29] for POD). These studies have employed the substructure technique to avoid calculating a complete basis when the domain leads to large matrices or increase precision on regions of interest. Finally, two studies^{30,31} used the BERM method with a branch basis when solving heat transfer problem in a substructured configuration. In continuation of these previous works, the aim of the present study is to develop the AROMM method for a shell geometry using the branch basis associated with a substructuring technique, to simulate the thermal behavior of a simplified part of an LNG tanker.

2 | PHYSICAL PROBLEM WITHOUT ANY THERMAL CONTACT RESISTANCE: THE ONE-PIECE DOMAIN FORMULATION

N_e enclosures are considered, each defined as a closed set of walls, containing a gas, and equipped with mechanical stiffeners. The thermal fields of the walls of these enclosures are governed by conduction phenomena in the walls and convective exchanges between the wall and the surrounding fluids (Figure 1).

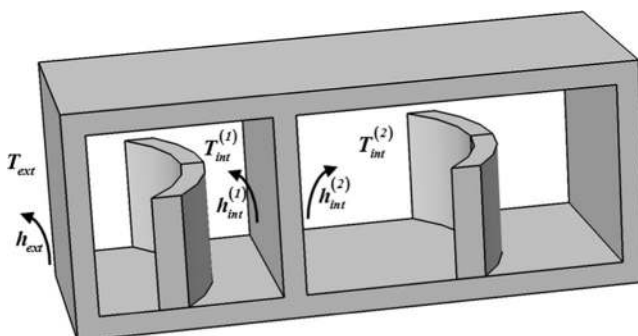


FIGURE 1 The considered geometry

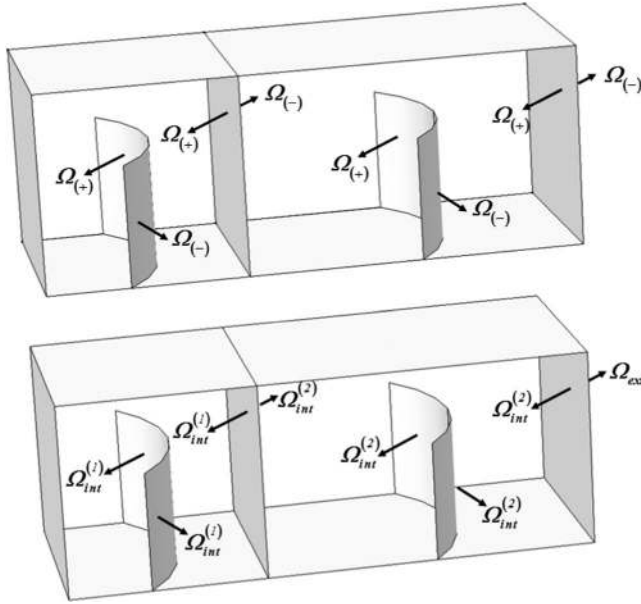


FIGURE 2 Analysis of borders of a shell element

Indoor temperatures $T_{int}^{(e)}$ are related to convective exchanges with all the walls. Assuming that the heat capacity of the internal fluid is negligible compared with that of the walls, a simple heat balance on the volume of gas provides the expression of indoor temperatures:

$$T_{int}^{(e)} = \frac{1}{\int_{\Omega_{int}^{(e)}} h_{int}^{(e)} d\Omega} \int_{\Omega_{int}^{(e)}} h_{int}^{(e)} T d\Omega. \quad (1)$$

If the temperature gradient in the thickness of the wall of the enclosure is negligible, it is possible to use a shell model (Figure 2), in which the temperature field depends only on local coordinates (η, ζ) for the plane Ω defined for the wall: $T(x, y, z) = T(\eta, \zeta)$. This domain Ω corresponds to the main surface of the shell and has two faces, characterized by normal vectors of opposite signs: $\Omega_{(+)}$ and $\Omega_{(-)}$ (Figure 2a). The weak formulation of the heat equation is then expressed as follows:

$$\int_{\Omega} e c \frac{\partial T}{\partial t} f d\Omega = - \int_{\Omega} e \lambda \vec{\nabla} T \cdot \vec{\nabla} f d\Omega + \int_{\Omega_{(+)}} \varphi f d\Omega + \int_{\Omega_{(-)}} \varphi f d\Omega, \quad (2)$$

where φ is the heat flux exchanged with the surrounding fluids, $e(M)$ is the thickness of the wall, which is not necessarily uniform on Ω , and $f \in H_1(\Omega)$ is the test function on Ω .

Faces $\Omega_{(+)}$ and $\Omega_{(-)}$ receive convective heat fluxes and can also be decomposed into the sum of the surfaces facing the outer side of the enclosure Ω_{ext} and those facing the interior volume of each enclosure $\Omega_{int}^{(e)}$ (Figure 2b):

$$\Omega = \Omega_{(+)} \cup \Omega_{(-)} = \left(\bigcup_{e=1}^{N_e} \Omega_{int}^{(e)} \right) \cup \Omega_{ext}. \quad (3)$$

Equation (2) finally becomes:

$$\int_{\Omega} ec \frac{\partial T}{\partial t} f d\Omega = - \int_{\Omega} e\lambda \vec{\nabla} T \cdot \vec{\nabla} f d\Omega + \sum_{e=1}^{N_e} \left\{ - \int_{\Omega_{int}^{(e)}} h_{int}^{(e)} T f d\Omega + \int_{\Omega_{int}^{(e)}} h_{int}^{(e)} T_{int}^{(e)}(T) f d\Omega \right\} - \int_{\Omega_{ext}} h_{ext} T f d\Omega + \int_{\Omega_{ext}} h_{ext} T_{ext} f d\Omega, \quad (4)$$

where $T_{int}^{(e)}$ is defined by relation (1).

3 | PHYSICAL PROBLEM WITH THERMAL CONTACT RESISTANCES: THE SUBSTRUCTURING METHOD

The method consists of splitting the geometry into N_d substructures $\Omega^{(k)}$ such as

$$\Omega = \bigcup_{k=1}^{N_d} \Omega^{(k)}. \quad (5)$$

As shown in Figure 3, subdomains $\Omega^{(i)}$ and $\Omega^{(j)}$ have N_{fc} shared boundaries, denoted as $\Gamma_{st}^{(l)}$, $1 \leq l \leq N_{fc}$ (Figure 3). The subscript of line l is associated unambiguously to the subscripts i and j of the two areas that are linked by this line.

The substructuring method applied to a shell model leads to particular boundaries that appear inside the considered domain (Figure 4). The borders $\Gamma_{st}^{(l)}$ can then be defined

- as classical external boundaries to a domain: $\Gamma_{st}^{(l)}$,
- as particular internal boundaries: $\Gamma_{st}^{(l)}$.

where

$$\begin{aligned} \Gamma_{st} &= \Gamma_{st}^{(e)} \cup \Gamma_{st}^{(i)} \\ \Gamma_{st}^{(e)} \cap \Gamma_{st}^{(i)} &= \emptyset. \end{aligned} \quad (6)$$

By considering that each border is characterized by a flux condition, Equation (2) for the considered subdomain $\Omega^{(k)}$ (Figure 3) is expressed as follows:

$$\begin{aligned} \int_{\Omega^{(k)}} ec \frac{\partial T^{(k)}}{\partial t} f^{(k)} d\Omega &= - \int_{\Omega^{(k)}} e\lambda \vec{\nabla} f^{(k)} \cdot \vec{\nabla} T^{(k)} d\Omega + \int_{\Omega_{(+)}^{(k)}} \varphi^{(k)} f^{(k)} d\Omega + \int_{\Omega_{(-)}^{(k)}} \varphi^{(k)} f^{(k)} d\Omega \\ &+ \int_{\Gamma_{st}^{(k)}} \varphi^{(k)} f^{(k)} d\Gamma. \end{aligned} \quad (7)$$

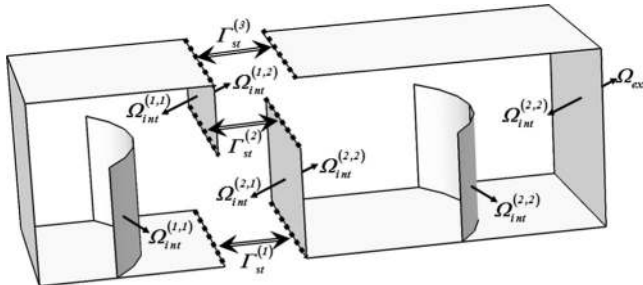


FIGURE 3 The substructuring principle

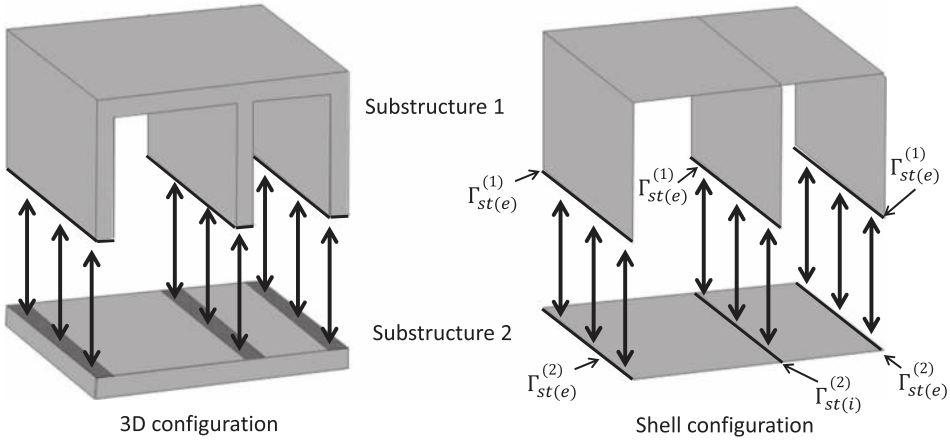


FIGURE 4 Substructuring problem in a shell geometry: Emergence of internal boundaries

As the two subdomains $\Omega^{(i)}$ and $\Omega^{(j)}$ exchange heat through each border $\Gamma_{st}^{(l)}$, the variational formulation of the heat transfer problem over the entire domain Ω is written as follows:

$$\begin{aligned} \sum_{k=1}^{N_d} \int_{\Omega^{(k)}} ec \frac{\partial T^{(k)}}{\partial t} f^{(k)} d\Omega &= - \sum_{k=1}^{N_d} \int_{\Omega^{(k)}} e\lambda \vec{\nabla} f^{(k)} \cdot \vec{\nabla} T^{(k)} d\Omega - \sum_{k=1}^{N_d} \int_{\Omega^{(k)}} \varphi^{(k)} f^{(k)} d\Omega \\ &- \sum_{k=1}^{N_d} \int_{\Omega^{(k)}} \varphi^{(k)} f^{(k)} d\Omega + \sum_{l=1}^{N_{jc}} \int_{\Gamma_{st}^{(l)}} (\varphi^{(i)} f^{(i)} + \varphi^{(j)} f^{(j)}) d\Gamma. \end{aligned} \quad (8)$$

The conservation of the heat flux leads to the classical relation between the flux and temperatures:

$$\varphi^{(i)} = -\varphi^{(j)} = \frac{e}{R_{TC}} (T^{(i)} - T^{(j)}) \equiv \frac{e}{R_{TC}} [[T]]^{(l)}, \quad (9)$$

where R_{TC} is a thermal contact resistance. From this relation, and considering the convective flux on $\Omega_{int}^{(k,e)}$ and Ω_{ext} , the variational formulation of the heat equation on the entire domain (Equation 2) is written as follows:

$$\begin{aligned} \sum_{k=1}^{N_d} \int_{\Omega^{(k)}} ec \frac{\partial T^{(k)}}{\partial t} f^{(k)} &= - \sum_{k=1}^{N_d} \int_{\Omega^{(k)}} e\lambda \vec{\nabla} T^{(k)} \cdot \vec{\nabla} f^{(k)} d\Omega - \sum_{k=1}^{N_d} \sum_{e=1}^{N_e} \int_{\Omega_{int}^{(k,e)}} h_{int} T^{(k)} f^{(k)} d\Omega \\ &- \sum_{k=1}^{N_d} \int_{\Omega_{ext}^{(k)}} h_{ext} T^{(k)} f^{(k)} d\Omega + \sum_{l=1}^{N_{jc}} \int_{\Gamma_{st}^{(l)}} \frac{e}{R_{TC}} [[T]]^{(l)} [[f]]^{(l)} d\Gamma \\ &+ \sum_{k=1}^{N_d} \sum_{e=1}^{N_e} \int_{\Omega_{int}^{(k,e)}} h_{int} T_{int}^{(k,e)}(T) f^{(k)} d\Omega + \sum_{k=1}^{N_d} \int_{\Omega_{ext}^{(k)}} h_{ext} T_{ext} f^{(k)} d\Omega, \end{aligned} \quad (10)$$

where $T_{int}^{(k,e)}(T)$ is defined by Equation (1).

The discretization of the problem defined by Equations (10) and (1) by Lagrange finite elements results in the following matrix problem (referred hereafter as detailed model):

$$\mathbf{C} \frac{d\mathbf{T}}{dt} = [\mathbf{K} + \mathbf{H}_{int} + \mathbf{H}_{ext} + \mathbf{J}_{st}] \mathbf{T} + \mathbf{U}_{cpl} \mathbf{T}_{int}(\mathbf{T}) + \mathbf{U}_0, \quad (11)$$

and

$$\mathbf{T}_{\text{int}}(\mathbf{T}) = \mathbf{D}\mathbf{T}. \quad (12)$$

The matrices of Equations (11) and (12) are sparse block matrices constructed from the finite-element matrices of each of the substructures. Construction of block sparse matrices is detailed in Appendix A. Block sparse matrices \mathbf{C} , \mathbf{K} , \mathbf{H}_{int} , \mathbf{H}_{ext} , of dimension (N, N) , are thermal inertia, conductivity, and accommodation matrices extern and intern, respectively, whereas matrix \mathbf{J}_{st} results from the coupling between substructures via the contact resistance. Matrix \mathbf{U}_{cpl} corresponds to the convective term with the air inside each enclosure area, whereas \mathbf{U}_0 is a vector representing the external known solicitations. \mathbf{D} is a matrix of dimension (N_e, N) giving us, from nodal temperature \mathbf{T} , the access to $\mathbf{T}_{\text{int}}(\mathbf{T})$, which is the vector containing the temperature of the air inside each enclosure. To avoid the manipulation of the dense matrix $\mathbf{H}_{\text{cpl}} = \mathbf{U}_{\text{cpl}}\mathbf{D}$, incompatible with the finite-element method, Equations (11) and (12) are solved iteratively.

4 | MODAL METHOD FOR THE SUBSTRUCTURING TECHNIQUE

4.1 | Principle

In modal methods for a single domain Ω , the temperature field $T(M, t)$ is projected on a basis (z_i, \mathbf{V}_i) of the space of the solution. Here, z_i is the eigenvalue and \mathbf{V}_i is the eigenvector for the i th element of the basis. When obtained numerically, the number N of modes computed is linked to the discretization: for P1 finite elements, N correspond to the mesh points number. This projection is written as follows:

$$T(M, t) = \sum_{i=1}^N x_i(t) V_i(M), \quad (13)$$

where x_i is the time-dependent amplitude, called the excitation state.

The principle of the modal substructuring technique is to compute a basis $(z_i^{(k)}, V_i^{(k)})$ for each substructure $\Omega^{(k)}$:

$$T^{(k)}(M, t) = \sum_{i=1}^{N^{(k)}} x_i^{(k)}(t) V_i^{(k)}(M). \quad (14)$$

4.2 | Branch basis

Among the different possible bases, the branch basis defined by Equations (15a) and (15b) for each substructure (k) is particularly adapted to the problem characterized by nonlinear boundary conditions,²³ as the branch vectors form a basis for the Hilbert space $H^1(\Omega)$.@@@

$$\forall M \in \Omega^{(k)}, \text{div} \left(\lambda_0 \vec{\nabla} V_i^{(k)} \right) = z_i^{(k)} c_0 V_i^{(k)}, \quad (15a)$$

$$\forall M \in \Gamma_{st}^{(k)}, \lambda_0 \vec{\nabla} V_i^{(k)} \vec{n} = -z_i^{(k)} \zeta V_i^{(k)}. \quad (15b)$$

The originality of this problem is the Steklov boundary condition, which depends on the eigenvalue $z_i^{(k)}$ and is independent of the boundary conditions of the real thermal problem. For a substructured problem in which common intern boundary $\Gamma_{st(i)}^{(k)}$ in the domain $\Omega^{(k)}$ may exist, an adapted eigenvalue problem to this condition and the shell model (thickness e_0) is proposed:

$$\forall M \in \Omega^{(k)}, e_0 \operatorname{div} \left(\lambda_0 \vec{\nabla} V_i^{(k)} \right) = z_i^{(k)} \left[e_0 c_0 V_i^{(k)} + \delta_{(\Gamma_{st(i)}^{(k)})} e_0 \zeta V_i^{(k)} \right], \quad (16a)$$

$$\forall M \in \Gamma_{st}^{(k)}, e_0 \lambda_0 \vec{\nabla} V_i^{(k)} \cdot \vec{n}_{\Gamma_{st(i)}^{(k)}} = -z_i^{(k)} e_0 \zeta V_i^{(k)}. \quad (16b)$$

where Γ boundaries are defined in Equation (6) and $\delta_{(\Gamma_{st(i)}^{(k)})}$ is the Dirac delta function defined by

$$\forall M \in \Gamma_{st(i)}^{(k)}, \delta_{(\Gamma_{st(i)}^{(k)})} = 1, \quad (17a)$$

$$\forall M \in \Omega^{(k)} \setminus \Gamma_{st(i)}^{(k)}, \delta_{(\Gamma_{st(i)}^{(k)})} = 0. \quad (17b)$$

The weak formulation for a shell model of Equation (16) is written in a compact form (for details, see Appendix C):

$$\forall f \in H_1(\Omega), \int_{\Omega^{(k)}} e_0 \lambda_0 \vec{\nabla} f^{(k)} \cdot \vec{\nabla} V_i^{(k)} d\Omega = -z_i^{(k)} \left(\int_{\Omega^{(k)}} e_0 c_0 V_i^{(k)} f^{(k)} d\Omega + \int_{\Gamma_{st}^{(k)}} e_0 \zeta V_i^{(k)} f^{(k)} d\Gamma \right). \quad (18)$$

To balance the two terms $\int_{\Omega^{(k)}} e_0 c_0 V_i^{(k)} f^{(k)} d\Omega$ and $\int_{\Gamma_{st}^{(k)}} e_0 \zeta V_i^{(k)} f^{(k)} d\Gamma$ in Equation (18), an appropriate choice of the Steklov coefficient ζ is given by the following:

$$\zeta = \frac{1}{\int_{\Gamma_{st}^{(k)}} e_0 d\Gamma} \int_{\Omega^{(k)}} e_0 c_0 d\Omega. \quad (19)$$

This special boundary condition reveals two types of modes. The first type is constituted of quasi-null modes on the boundary but not on the domain, and the second one of quasi-null modes on the domain but not on the boundary. Examples of such modes are given in Figure 5. In this way, the branch modes form a basis for any thermal problem, irrespective of the boundary conditions. For a substructured problem in which a contact resistance R_{TC} appears, this second type of mode allows to link the temperature “sub-fields” on the interface.

4.3 | Amalgam reduction

From the original branch basis $(z_i^{(k)}, V_i^{(k)})$, the objective of the modal reduction is to build a reduced basis $(\tilde{z}_i^{(k)}, \tilde{V}_i^{(k)})$, of dimension $\tilde{N}^{(k)} \ll N^{(k)}$, which permits to approach correctly the thermal field by the relation:

$$T^{(k)}(M, t) \approx \sum_{i=1}^{\tilde{N}^{(k)}} \tilde{x}_i^{(k)}(t) \tilde{V}_i^{(k)}(M). \quad (20)$$

The reduction step is performed by the amalgam reduction method. Unlike other techniques,^{19,32,33} all original modes are retained, because modes $V_i^{(k)}$ are amalgamated:

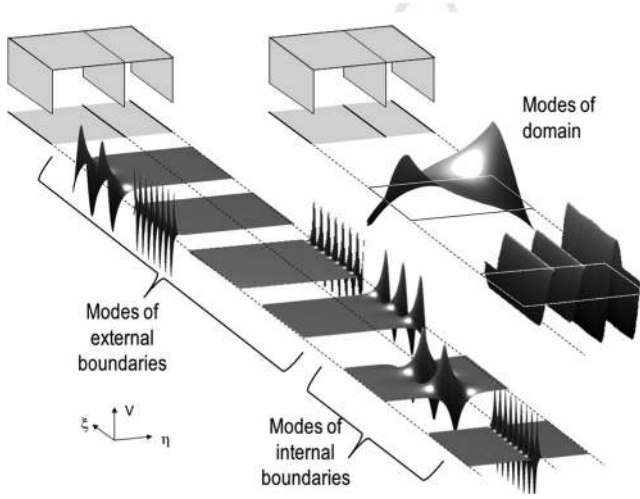


FIGURE 5 Examples of branch modes for a substructure corresponding to a single plate

$$\forall i \in \{1, \dots, \tilde{N}^{(k)}\} \tilde{V}_i^{(k)}(M) = \sum_{p=1}^{N_i^{(k)}} \alpha_{i_p}^{(k)} V_{i_p}^{(k)}. \quad (21)$$

To ensure the orthogonality of the reduced basis, each eigenvector V_i is used only once.

The distribution of the original modes $V_i^{(k)}$ in the reduced basis $\tilde{V}_i^{(k)}$ and the calculation of the weighting coefficient $\alpha_{i_p}^{(k)}$ are obtained from excitation states $x_i^{(k)}$ of each eigenvectors of the complete basis, for a physical reference case, characterized by constant parameters c_{ref} , λ_{ref} , and h_{ref} . Detailed calculations are developed in the study reported in Reference [23].

For each subdomain $\Omega^{(k)}$, a reduced basis $(\tilde{z}_i^{(k)}, \tilde{V}_i^{(k)})$, of dimension $\tilde{N}^{(k)}$, is obtained. The extension of each basis on the whole domain is obtained by extending each eigenvector by zero on the other subdomains. Each vector then defined on the whole domain can be written as $\hat{V}_i^{(k)}$.

The substructured reduced basis of the whole domain Ω is then constituted by all modes defined as above. We can then write that all N_d thermal fields of each subdomain $\Omega^{(k)}$ can be projected on the substructured modal basis, which is thus defined as follows:

$$T(M, t) \approx \hat{T}(M, t) = \sum_{p=1}^{\tilde{N}} \hat{x}_p(t) \hat{V}_p(M), \quad (22)$$

where

$$\hat{N} = \sum_{k=1}^{N_d} \tilde{N}^{(k)}. \quad (23)$$

4.4 | Substructured modal formulation

The substructured modal formulation is obtained by using the temperature projection on the basis (Equation 22) in the variational formulation (Equation 10) and by replacing the test

function f by the eigenvector \widehat{V}_q of the substructured basis. We obtain the following equation, in which the operators are bilinear, symmetric, and positive definite:

$$\begin{aligned} \sum_{p=1}^{\widehat{N}} \sum_{k=1}^{N_d} \int_{\Omega^{(k)}} e c \widehat{V}_p \widehat{V}_q d\Gamma \frac{\partial \widehat{x}_p}{\partial t} = & - \sum_{p=1}^{\widehat{N}} \sum_{k=1}^{N_d} \int_{\Omega^{(k)}} e \lambda \vec{\nabla} \widehat{V}_p \cdot \vec{\nabla} \widehat{V}_q d\Omega \widehat{x}_p \\ & - \sum_{p=1}^{\widehat{N}} \sum_{k=1}^{N_d} \left(\sum_{e=1}^{N_e} \int_{\Omega^{(k,e)}} h_{int} \widehat{V}_p \widehat{V}_q d\Omega + \int_{\Omega^{(k)}} h_{ext} \widehat{V}_p \widehat{V}_q d\Omega \right) \widehat{x}_p \\ & + \sum_{p=1}^{\widehat{N}} \left(\sum_{l=1}^{N_{fc}} \int_{\Gamma_{st}^{(l)}} \frac{e}{R_{TC}} [[\widehat{V}_p]]^{(l)} [[\widehat{V}_q]]^{(l)} d\Gamma \right) \widehat{x}_p \\ & + \sum_{p=1}^{\widehat{N}} \sum_{k=1}^{N_d} \left(\sum_{e=1}^{N_e} \frac{1}{\int_{\Omega^{(k,e)}} h_{int} d\Omega} \int_{\Omega^{(k,e)}} h_{int} \widehat{V}_p d\Omega \int_{\Omega^{(k,e)}} h_{int} \widehat{V}_q d\Omega \right) \widehat{x}_p \\ & + \sum_{p=1}^{\widehat{N}} \sum_{k=1}^{N_d} \int_{\Omega^{(k)}} h_{ext} T_{ext} \widehat{V}_q d\Omega. \end{aligned} \quad (24)$$

According to the numerical formulation (Equations 11 and 12):

$$\widehat{\mathbf{V}}^t \mathbf{C} \widehat{\mathbf{V}} \frac{d\widehat{\mathbf{X}}}{dt} = \widehat{\mathbf{V}}^t [\mathbf{K} + \mathbf{H}_{int} + \mathbf{H}_{ext} + \mathbf{J}_{st}] \widehat{\mathbf{V}} \widehat{\mathbf{X}} + \widehat{\mathbf{V}}^t \mathbf{U}_{cpl} \mathbf{D} \widehat{\mathbf{V}} \widehat{\mathbf{X}} + \widehat{\mathbf{V}}^t \mathbf{U}_0, \quad (25)$$

where $\widehat{\mathbf{V}}[N, \widehat{N}]$ is the matrix containing the \widehat{N} discrete vectors \widehat{V}_p . Construction of reduced matrix $\widehat{\mathbf{V}}[N, \widehat{N}]$ and vector $\widehat{\mathbf{X}}$ is detailed in Appendix B.

In a compact form:

$$\mathbf{L} \frac{d\widehat{\mathbf{X}}}{dt} = \mathbf{M} \widehat{\mathbf{X}} + \mathbf{N}. \quad (26)$$

Matrices \mathbf{L} and \mathbf{M} are dense and with dimension $(\widehat{N}, \widehat{N})$.

5 | APPLICATION

5.1 | Physical problem

The application is a simplified portion of the structure of an LNG carrier, the cofferdam, which corresponds to a mechanical retaining element between two LNG tanks (Figure 6). The configuration studied consists of $N_e = 20$ enclosures (Figure 7A), each containing four stiffeners (Figure 7B). The dimension of the simplified cofferdams is around 4 m, instead of 30 m, for a real ship's shell. The cofferdam walls and stiffeners are characterized by different thicknesses e (1–3 cm) and constant thermal characteristics ($\lambda = 45 \text{ W} \cdot \text{m}^{-1} \cdot \text{K}^{-1}$, $c = 3.4 \times 10^6 \text{ J} \cdot \text{m}^{-3} \cdot \text{K}^{-1}$). To keep the walls at an acceptable temperature above 5°C , despite the proximity of the LNG tanks, a heating system is positioned through the cofferdam. It is composed of two steel pipes (see

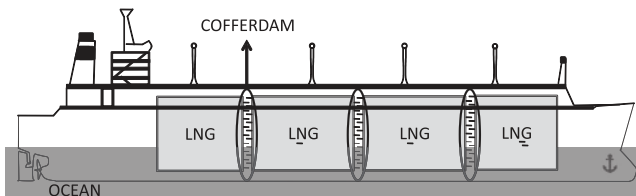


FIGURE 6 A schematic view of a liquefied natural gas (LNG) tanker

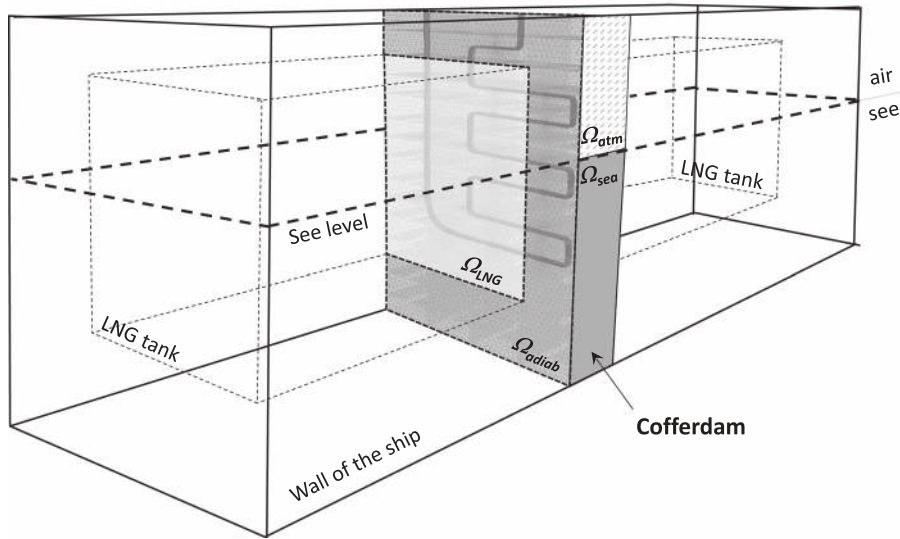


FIGURE 7 The cofferdam and its internal boundaries conditions. (A) Complete cofferdam, (B) one enclosure, and (C) details of the tubes

Figure 7A) in which glycol–water maintained at 65°C circulates. As shown in Figure 7C, these tubes come through the walls of the cofferdam, along a border Γ_{st} . Along this border, the contact between pipes and walls is imperfect, which is then characterized by a thermal contact resistance $R_{TC} = 1 \text{ K}\cdot\text{m}^2\cdot\text{W}^{-1}$.

The thermal behavior of the cofferdam when a shutdown of the heating circuit appears is simulated. The initial condition is the nominal operating temperature, and the simulation duration is $3 \times 10^4 \text{ s}$.

The external boundary conditions are those from the U.S. Coast Guard (U.S.A. federal agency imposing computing standards), which are represented in Figure 8. Given the uncertainties that exist in the values of various convection coefficients, the goal is to perform a sensitivity analysis of the cofferdam's thermal comportment to these coefficients.

The outer surfaces can be divided into several sub-boundaries:

- Ω_{atm} is in contact with the atmosphere (h_{atm} variable, $T_{atm} = -18^{\circ}\text{C}$),
- Ω_{sea} is in contact with the sea (h_{sea} variable, $T_{sea} = 0^{\circ}\text{C}$),
- Ω_{LNG} is in contact with the insulated tank containing the LNG (h_{LNG} variable, $T_{LNG} = -163^{\circ}\text{C}$), and
- Ω_{adiab} corresponds to the surface in contact with other enclosures of the ship, for which an adiabatic condition is applied.

Concerning the values of these convective coefficients, three cases are considered and presented in Table 1:

The heat supplied by the glycol–water to the tubes is simulated during normal operation by a convective flux: $h_{bri} = 1000 \text{ W}^{-2}\cdot\text{K}^{-1}$, $T_{bri} = 65^{\circ}\text{C}$ (Figure 7C). During the shutdown, we consider that no more heat is brought and these tubes are cooled by convective exchange with the surrounding enclosures through which they pass.

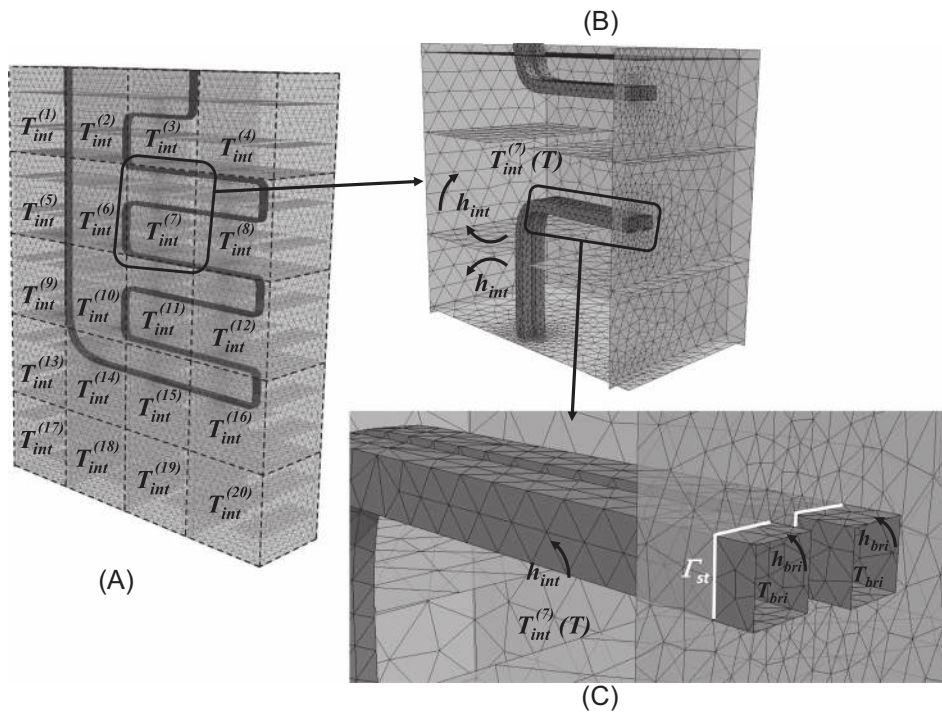


FIGURE 8 The cofferdam and its external boundaries conditions

These external thermal loads (atmosphere, sea, glycol–water, and LNG) are globally noted as h_{ext} and T_{ext} .

As presented in Figure 7B, a convective heat exchange between the inner walls of each enclosure (including the walls of the tubes passing through it) and indoor air (whose temperature is unknown and depends on its surroundings) is made via a constant exchange coefficient h_{int} . As for the other convective coefficients, three values are used (Table 1).

5.2 | Hypotheses

Considering the above characteristics, the following facts are revealed:

- the maximum Biot Number $Bi = \frac{h e}{2 \lambda} \leq 0.06$ (with $e = 3\text{cm}$ and $h = 168 \text{W} \cdot \text{m}^{-2} \cdot \text{K}^{-1}$),
- the surface variation between the inside and the outside is negligible, and

TABLE 1 Values of the various convection coefficients used ($\text{W} \cdot \text{m}^{-2} \cdot \text{K}^{-1}$)

	h_{int}	h_{sea}	h_{atm}	h_{LNG}
Minimum configuration: $\beta = 0.6$	2.4	72	8.4	0.12
Intermediate configuration: $\beta = 1$	4	120	14	0.20
Maximum configuration: $\beta = 1.4$	5.6	168	19.6	0.28

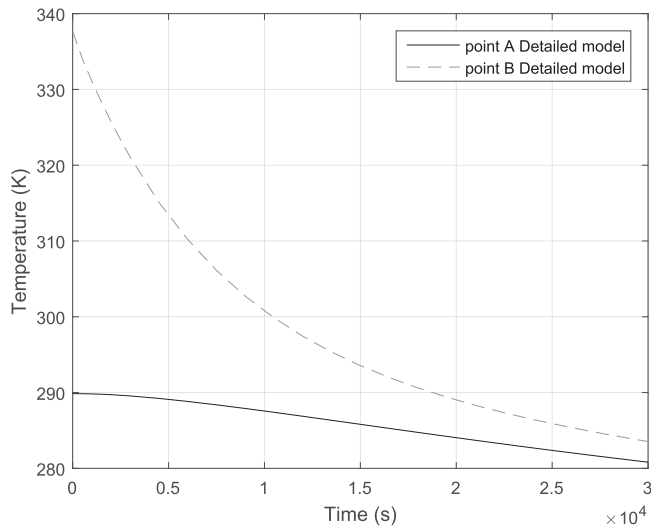


FIGURE 9 Temporal evolution of the temperature on points A and B

- the ratio of thermal capacity between the wall and the gas inside is $\frac{(cVo)_{wall}}{(cVo)_{gas}} \approx 200$ (where Vo is the volume).

Thus, first, it can be considered that the shell model can be used and, second, that the thermal inertia of the gas in the enclosures may not be taken into account. The physical model described above can be applied.

6 | RESULTS AND DISCUSSION

6.1 | Detailed model

A finite-element model (the detailed model) will be referred to quantify the effectiveness of the reduced model (Equations 11 and 12). In the processed application, a sensitivity analysis showed that a mesh of 21,548 nodes in the simplified cofferdam and 6600 nodes per pipe is required. The resolution of the transient problem over a period of 3×10^4 s is performed by a CPU time of 60 s. In case $\beta = 1$, Figure 9 allows to visualize the cooling of the cofferdam (point A shown in Figure 8) and heating pipes (point B). The inertia due to the heating tubes keeps the temperature of the stiffeners near 290K for about an hour, and therefore delays the risk of rupture.

6.2 | A reduced substructured model for physical thermal resistances: The 3ST model

A sensitivity analysis on the reduction order has been conducted. To quantify its results, the following quantities are defined:

$$\langle \varepsilon \rangle = \frac{1}{V} \frac{1}{\tau} \frac{\int_{\tau} \int_{\Omega} |T - \hat{T}| d\Omega}{\max_{\tau, \Omega}(T) - \min_{\tau, \Omega}(T)}, \varepsilon_{\max} = \frac{\max_{\tau, \Omega} |T - \hat{T}|}{\max_{\tau, \Omega}(T) - \min_{\tau, \Omega}(T)},$$

where τ is the simulation duration and V the volume of domain Ω .

In this model, the division into substructures follows the physical division, with appearance of three substructures: the cofferdam (*ST1*) and the two heating pipes (*ST2* and *ST3*). The reduced model is obtained by using the reference configuration $\beta = 1$ for the amalgam procedure. For three selected configurations (Table 1), different modal simulations are carried out, keeping 40 modes for each heating tube and varying the number of modes for the cofferdam. The construction of the modal model (computation of the basis and reduction) is performed offline, which requires a calculation time of 1642 s.

Figure 10 shows the evolution of the error on points A and B for the configuration $\beta = 1.4$ with a reduced model using 200 modes (RM200). It clearly appears that the error is larger for the first steps of simulation, which tends to stabilize at a value less than 0.1 K. This type of behavior is typical of reduced models, as the reduction does not keep the momentum of the fastest modes.

All results are presented in terms of average and maximum temperature deviations from the detailed model and computational gain in Table 2.

When the boundary conditions for the simulation match those used for reduction ($\beta = 1$), the difference between reduced and detailed models is already very low with only 120 modes (compared with 34,748 nodes of the initial mesh), with a maximum deviation of 0.73 K, an average deviation of 0.023 K, and a gain in terms of computation time of the order of 60, thus showing the effectiveness of the method for problems characterized by structures coupled by a thermal contact resistance.

When the boundary conditions are different from those used during reduction ($\beta = 0.6$ and $\beta = 1.4$), performance degrades: to maintain a maximum error of less than 1 K, the reduced model must contain between 200 and 240 modes, which limits the gain in computation time of

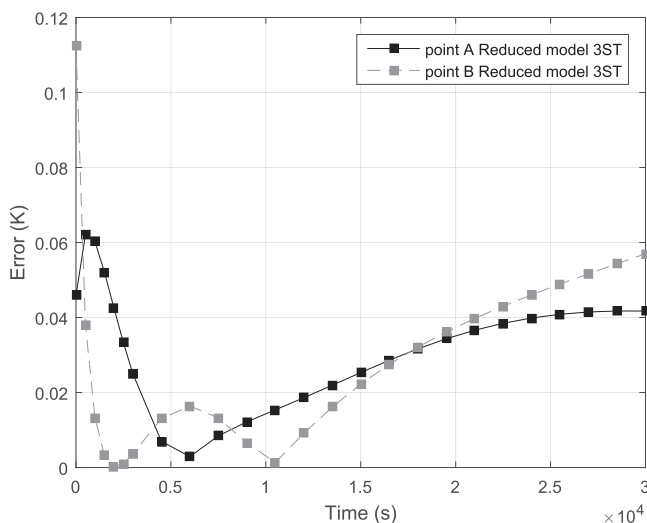


FIGURE 10 A 3ST substructured model: Temporal evolution of the deviation between detailed and reduced RM200 models (for $\beta = 1.4$)

TABLE 2 Maximum and average absolute error for different reduction orders for 3 ST

Model order	Error (K)						Gain in computation time
	$\beta = 0.6$		$\beta = 1$		$\beta = 1.4$		
	ε_{max}	$\bar{\varepsilon}$	ε_{max}	$\bar{\varepsilon}$	ε_{max}	$\bar{\varepsilon}$	
120 (40,40,40)	2.2	0.15	0.73	0.023	1.82	0.110	58
140 (60,40,40)	1.11	0.13	0.40	0.016	1.23	0.098	48
160 (80,40,40)	1.14	0.11	0.33	0.012	0.83	0.083	40
200 (120,40,40)	1.19	0.085	0.18	0.008	0.81	0.063	27
240 (160,40,40)	0.796	0.071	0.17	0.007	0.63	0.052	20

20–27. The average errors for these models are extremely low (they are between 0.063 and 0.085 K), thus indicating that the maximum error remains isolated in space and time.

6.3 | A reduced substructured model for fictitious thermal resistance: The 6ST model

In addition to the two pipes, the cofferdam has been artificially divided into four substructures shown in Figure 11 and coupled together by an artificial contact resistance. It is then checked if the method is able to reduce such a problem.

The first step is to find an optimal value for the fictitious thermal contact resistance. Indeed, an excessive value of the fictitious resistance biases results by introducing a very important nonphysical temperature jump. However, due to the reduction of the modal basis, imposing an extremely low-temperature jump at the interface induces a significant error in the calculation of the heat flux, and therefore significant temperature differences in the interface as well as in

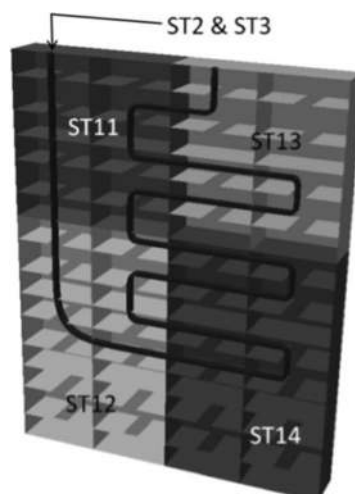
**FIGURE 11** A virtual division of the cofferdam

TABLE 3 The influence of the value of the fictitious contact resistance on the accuracy of the model for the case $\beta = 1.4$

R_{TC} ($\text{m}^2 \cdot \text{K} \cdot \text{W}^{-1}$)	Number of modes					
	240 (4×40 , 2×40)		160 (4×20 , 2×40)		120 (4×10 , 2×40)	
	ε_{\max} (K)	ε (\bar{K})	ε_{\max} (K)	ε (\bar{K})	ε_{\max} (K)	ε (\bar{K})
10^{-3}	2.72	0.095	2.35	0.128	2.12	0.162
2×10^{-5}	0.96	0.076	1.06	0.119	2.06	0.158
10^{-4}	0.96	0.076	1.01	0.123	1.92	0.165
5×10^{-5}	0.97	0.078	0.97	0.128	1.70	0.176
2×10^{-5}	1.02	0.083	1.57	0.137	1.82	0.195
10^{-5}	1.07	0.088	2.37	0.144	2.09	0.212
5×10^{-6}	1.13	0.094	3.25	0.153	3.19	0.233
10^{-6}	1.73	0.116	5.47	0.183	6.61	0.353

the domain. For the case $\beta = 1.4$, a sensitivity analysis on the value of the RTC has been conducted for different orders of reduction. Results are presented in Table 3.

It is first noted that for a given reduction order, depending on the chosen criterion (ε_{\max} or $\bar{\varepsilon}$), the optimum value of the contact resistance is not the same. In addition, the optimum value for a given criterion changes depending on the order of reduction. However, there is a whole range (roughly $5 \times 10^{-5} < R_{TC} < 10^{-4} \text{K} \cdot \text{m}^2 \cdot \text{W}^{-1}$) on which the change in spreads is low, indicating that an order of magnitude is sufficient. The value $R_{TC} = 10^{-4} \text{K} \cdot \text{m}^2 \cdot \text{W}^{-1}$ has been chosen. For the used steel ($k = 45 \text{W} \cdot \text{m}^{-2} \cdot \text{K}^{-1}$), this resistance corresponds to a thickness equal to 4.5 mm. This optimum resistance corresponds to an acceptable error of temperature jump at the interface between the substructures, considering the overall error linked to the use of a reduced model.

With $R_{TC} = 10^{-4} \text{K} \cdot \text{m}^2 \cdot \text{W}^{-1}$, several simulations are performed for the three configurations specified in Table 1 and for different reduction orders. As before, the order of reduction of each tube is kept constant (40 modes).

Figure 12 shows the time evolution of the difference between reduced and detailed model at points A and B (see Figure 2) for both divisions (physical and artificial) with 200 modes and $\beta = 1.4$. The evolution of the errors at these points is similar to that obtained for the model 3ST.

Figure 13 presents the overall results of these tests. When both divisions are compared, following the number of modes, the second splitting seems less relevant, as for $\beta = 1$ and 160 modes, for example, maximum and average deviations are about two times higher. This is easily explained as follows: as each substructure requires a minimum number of modes to reproduce a temperature field, increasing the number of substructures increases the total number of modes.

However, it is also noted that for a same order of reduction, the computation time is lower for the 6ST model than for the 3ST model. It seems as if the increase of the number of substructures leads to a weaker computation time. This can be explained by the nature of matrices: Figure 14 presents the value of the coefficients of the matrix \mathbf{M} (see Equation 26) for both configurations (3ST and 6ST). For the model 6ST, the matrix \mathbf{M} consists of small blocks (in comparison with the matrix \mathbf{M} of the model 3ST). The diagonal blocks corresponding to the

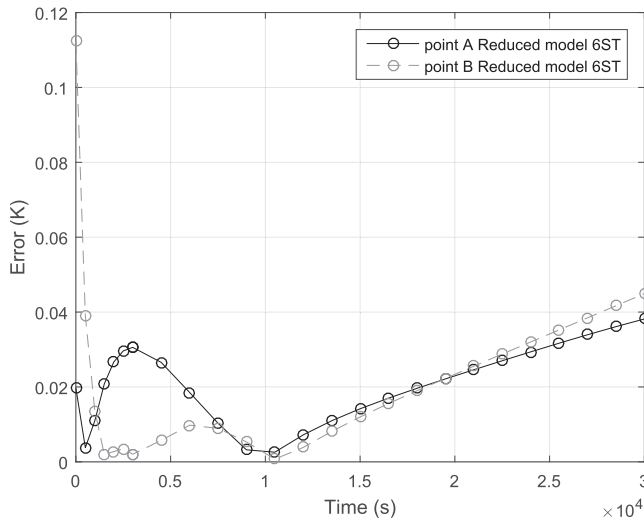


FIGURE 12 A 6ST substructured model: Temporal evolution of the deviation between detailed and reduced RM200 models (for $\beta = 1.4$)

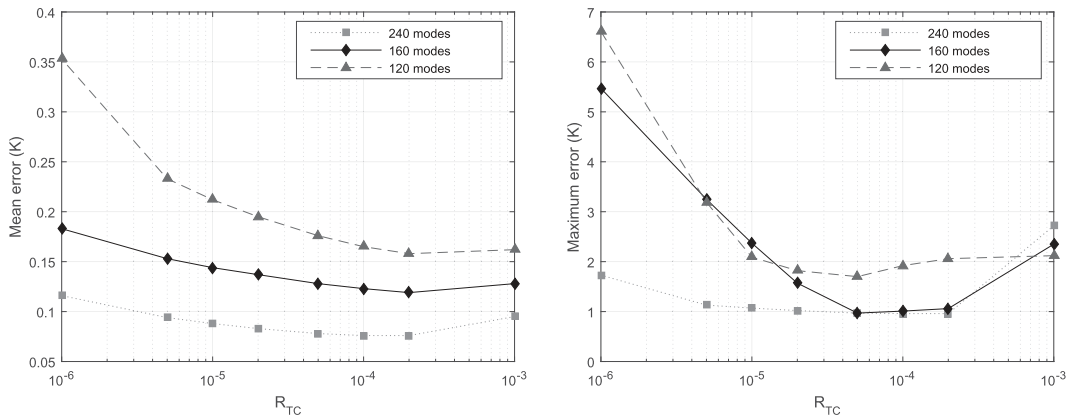


FIGURE 13 Maximum and average absolute error for different reduction orders for 6 ST

various substructures generally have higher values than non-diagonal blocks that correspond to the coupling between the substructures. The matrix resolution is achieved by BLAS and LAPACK libraries, which use partition block matrices. The matrix structure of the substructured problem is well suited to this kind of partition, as the substructure naturally leads blocks that contain zero or low values.

Thus, for a same order of reduction, the use of artificial splitting leads to

- an increase in maximum error and
- a decrease in CPU time.

Figure 15 represents the errors evolution versus the gain in computation time. Concerning the mean error $\bar{\epsilon}$:

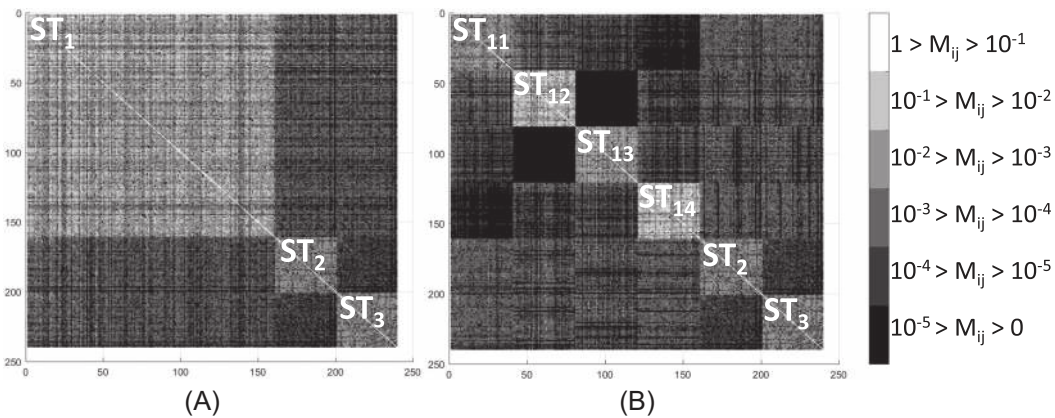


FIGURE 14 Matrix M. (A) 3ST and (B) 6ST

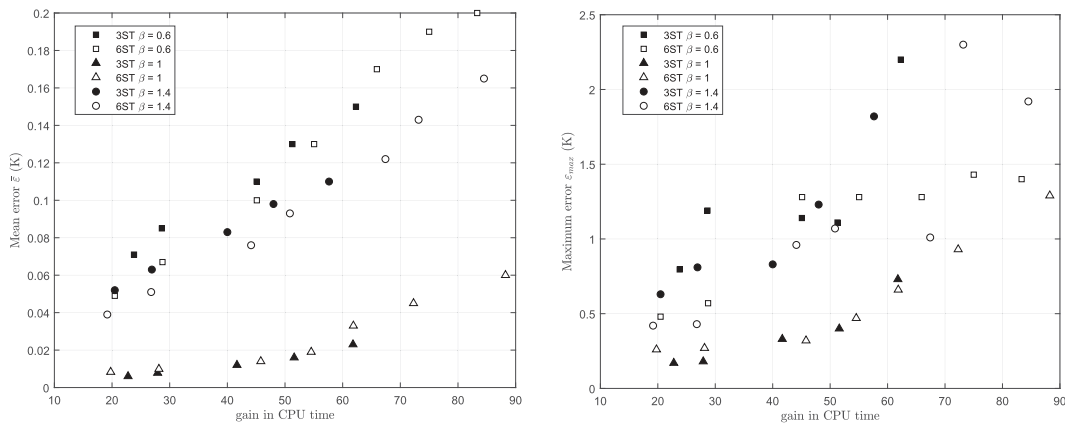


FIGURE 15 A comparison between the one-body and the substructured cofferdams

- For configuration $\beta = 1$ (for which the simulated thermal problem is the same as the one used for the amalgam procedure), both curves (3ST and 6ST) are coincident.
- In other cases, same precision requires more computational time for the 3ST model than for the 6ST model.

Regarding the maximum errors, the trend is the same, with more chaotic evolutions.

7 | CONCLUSION

The first objective of this paper was to study a substructured reduced model for a geometry made up of many thermal enclosures coupled together when the imperfect contact between different components reveals a temperature jump at the interface. We have shown the efficiency of this method, as for a different problem than the reference one, the maximum

deviation from Lagrange finite-element model is less than 1°C, while being 60 times faster. The entrance ticket of this model is the initial base computation on which the amalgamated base is built.

The second objective was to study the relevance of this technique for an artificial division of an initially continuous domain. The results are very satisfactory: the artificial cut allows a gain in computation time of the reduced model calculation without additional cost of error and time during simulation. Furthermore, with this substructured model, the time to create the reduced model is reduced by a factor 4, compared with the original case with physical separation.

This study, thus, demonstrated the effectiveness of the substructured modal method, which could be extended to the cofferdam in all its geometrical complexity and the entire ship structure.

CONFLICT OF INTERESTS

The authors declare that there are no conflict of interests.

DATA AVAILABILITY STATEMENT

The data that support the findings of this study are available from the corresponding author upon reasonable request.

NOMENCLATURE

VARIABLES

c	thermal heat capacity, $\text{J}\cdot\text{m}^{-3}\cdot\text{K}^{-1}$
e	wall thickness, m
ε_{\max}	maximum error over space and time, K
$\bar{\varepsilon}$	mean error, K
f	test function
φ	heat flux, $\text{W}\cdot\text{m}^{-2}$
h	heat exchange coefficient, $\text{W}\cdot\text{m}^{-2}\cdot\text{K}^{-1}$
λ	thermal conductivity, $\text{W}\cdot\text{m}^{-1}\cdot\text{K}^{-1}$
M	point of space (x,y,z), m
\vec{n}	normal
N	dimension of a substructure of the FE problem
\tilde{N}	dimension of a reduced base of a substructure k
\hat{N}	dimension of a global reduced problem
N_d	number of substructures
N_e	number of enclosures
N_{fc}	number of shared boundaries
R_{TC}	thermal contact resistance, $\text{K}\cdot\text{m}^2\cdot\text{W}^{-1}$
t	times, s
$T_{int}^{(e)}$	indoor temperature of enclosure e, K
$T(t, M)$	temperature of point M at t time, K
$V_i(M)$	Value of ith mode at point M, K
$x(t)$	modal amplitude at t time
z	eigenvalue, s^{-1}
ζ	Steklov number, $\text{J}\cdot\text{m}^{-2}\cdot\text{K}^{-1}$

SPECIAL

Δ	Laplace operator, m^{-2}
$\vec{\nabla}$	gradient operator, m^{-1}
Ω	domain
Γ	boundaries

MATRICES

D	transformation matrix from nodal to air temperatures
C	thermal inertia matrix, $\text{J}\cdot\text{K}^{-1}$
H	Accommodation matrix, $\text{W}\cdot\text{K}^{-1}$
J_{st}	Coupling matrix between substructures, $\text{W}\cdot\text{K}^{-1}$
K	Conductivity matrix, $\text{W}\cdot\text{K}^{-1}$
U_{cpl}	Matrix of convecting exchange with the air inside, $\text{W}\cdot\text{K}^{-1}$

VECTORS

T	temperature, K
U₀	vector of external solicitations, W
V	matrix of modes, K
X	vector of states

SUPERSCRIPTS

$\tilde{\circ}$	reduced notation of a substructure
$\hat{\circ}$	global reduced notation
\circ_e	enclosure e
\circ_k	substructure k
\circ_l	shared boundary l

REFERENCES

1. Sambou V, Lartigue B, Monchoux F, Adj M. Theoretical and experimental study of heat transfer through a vertical partitioned enclosure: application to the optimization of the thermal resistance. *Appl Therm Eng.* 2008;28(5):488-498.
2. Corcione M, Cianfrini M, Quintino A. Enhanced natural convection heat transfer of nanofluids in enclosures with two adjacent walls heated and the two opposite walls cooled. *Int J Heat Mass Transfer.* 2015;88:902-913.
3. Li LP, Wu ZG, He YL, Lauriat G, Tao WQ. Optimization of the configuration of 290x140x90 hollow clay bricks with 3-D numerical simulation by finite volume method. *Energy Build.* 2008;40(10):1790-1798.
4. Jaffal I, Inard C, Bozonnet E. Toward integrated building design: a parametric method for evaluating heating demand. *Appl Therm Eng.* 2012;40:267-274.
5. Gossard D, Lartigue B. Three-dimensional conjugate heat transfer in partitioned enclosures: determination of geometrical and thermal properties by an inverse method. *Appl Therm Eng.* 2013;54(2):549-558.
6. Harish VSKV, Kumar A. Reduced order modeling and parameter identification of a building energy system model through an optimization routine. *Appl Energy.* 2016;162:1010-1023.
7. Kircher KJ, Zhang KM. On the lumped capacitance approximation accuracy in RC network building models. *Energy Build.* 2015;108:454-462.
8. Jeffers AE. Heat transfer element for modeling the thermal response of non-uniformly heated plates. *Finite Elem Anal Des.* 2013;63:62-68.
9. An C, Su J. Lumped models for transient thermal analysis of multilayered composite pipeline with active heating. *Appl Therm Eng.* 2015;87:749-759.
10. Jeffers AE, Beata PA. Generalized shell heat transfer element for modeling the thermal response of non-uniformly heated structures. *Finite Elem Anal Des.* 2014;83:58-67.

11. Voldoire F. Formulation d'un modèle de thermique pour les coques minces, R3.11.01.: EDF; 2013.
12. Zhang X, Xiang H. A fast meshless method based on proper orthogonal decomposition for the transient heat conduction problems. *Int J Heat Mass Transfer*. 2015;84:729-739.
13. Ghosh R, Joshi Y. Error estimation in POD-based dynamic reduced-order thermal modeling of data centers. *Int J Heat Mass Transfer*. 2013;57(2):698-707.
14. He X, Kong Q, Xiao Z. Fast simulation methods for dynamic heat transfer through building envelope based on model-order-reduction. *Procedia Eng*. 2015;121:1764-1771. The 9th International Symposium on Heating, Ventilation and Air Conditioning (ISHVAC) joint with the 3rd International Conference on Building Energy and Environment (COBEE), 12-15 July 2015, Tianjin, China.
15. Ryckelynck D. A priori hyperreduction method: an adaptive approach. *J Comput Phys*. 2005;202(1):346-366.
16. Berger J, Guernouti S, Woloszyn M, Chinesta F. Proper generalised decomposition for heat and moisture multizone modelling. *Energy Build*. 2015;105:334-351.
17. Rouizi Y, Girault M, Favennec Y, Petit D. Model reduction by the Modal Identification Method in forced convection: application to a heated flow over a backward-facing step. *Int J Therm Sci*. 2010;49(8):1354-1368.
18. Videcoq E, Girault M, Bouderbala K, Nouira H, Salgado J, Petit D. Parametric investigation of Linear Quadratic Gaussian and Model Predictive Control approaches for thermal regulation of a high precision geometric measurement machine. *Appl Therm Eng*. 2015;78:720-730.
19. Salgon JJ, Neveu A. Application of modal analysis to modelling of thermal bridges in buildings. *Energy Build*. 1987;10(2):109-120.
20. Gao Y, Roux JJ, Teodosiu C, Zhao LH. Reduced linear state model of hollow blocks walls, validation using hot box measurements. *Energy Build*. 2004;36(11):1107-1115.
21. Gaume B, Joly F, Quémener O. Modal reduction for a problem of heat transfer with radiation in an enclosure. *Int J Heat Mass Transfer*. 2019;141:779-788.
22. Grosjean S, Gaume B, Joly F, Vera K, Neveu A. A modal substructuring method for non-conformal mesh. Application to an electronic board. *Int J Therm Sci*. 2020;152:106298.
23. Quemener O, Neveu A, Videcoq E. A specific reduction method for the branch modal formulation: application to a highly non-linear configuration. *Int J Therm Sci*. 2007;46(9):890-907.
24. Videcoq E, Quemener O, Lazard M, Neveu A. Heat source identification and on-line temperature control by a Branch Eigenmodes Reduced Model. *Int J Heat Mass Transfer*. 2008;51(19):4743-4752.
25. Videcoq E, Lazard M, Quemener O, Neveu A. Online temperature prediction using a branch eigenmode reduced model applied to cutting process. *Numer Heat Transf A Appl*. 2009;55(7):683-705.
26. Petit D, Hachette R. Model reduction in linear heat conduction: use of interface fluxes for the numerical coupling. *Int J Heat Mass Transfer*. 1998;41(21):3177-3189.
27. Flament B, Bourquin F, Neveu A. Synthèse modale: une méthode de sousstructuration dynamique pour la modélisation des systèmes thermiques linéaires. *Int J Heat Mass Transfer*. 1993;36(6):1649-1662.
28. Ménéz C, Roux JJ, Virgone J. Modelling heat transfers in building by coupling reduced-order models. *Build Environ*. 2002;37(2):133-144.
29. Kerfriden P, Gouy O, Rabczuk T, Bordas SPA. A partitioned model order reduction approach to rationalise computational expenses in nonlinear fracture mechanics. *Comput Methods Appl Mech Eng*. 2013;256:169-188.
30. Laffay PO, Quémener O, Neveu A, Elhajjar B. The modal substructuring method: An efficient technique for large-size numerical simulations. *Numer Heat Transfer B Fund*. 2011;60(4):278-304.
31. Laffay PO, Quémener O, Neveu A. Developing a method for coupling branch modal models. *Int J Therm Sci*. 2009;48(6):1060-1067.
32. Sicard P, Bacot A, Neveu J. Analyse modale des phénomènes thermiques en régime variable dans le bâtiment. *Rev Gen Therm*. 1984;267:189-201.
33. Sicard J, Bacot P, Neveu A. Analyse modale des échanges thermiques dans le bâtiment. *Int J Heat Mass Transfer*. 1985;28(1):111-123.

APPENDIX A: MATRICES CONSTRUCTION OF FE PROBLEM

Sparse matrices \mathbf{C} , \mathbf{K} , \mathbf{H}_{int} , \mathbf{H}_{ext} have a block diagonal and square structure of dimension $[N \times N]$. Each block is a classical finite-element matrix. For example, matrix \mathbf{C} can be written as follows:

$$\mathbf{C} = \begin{bmatrix} \mathbf{C}^{(1)} & 0 & \cdots & \cdots & \cdots & 0 \\ 0 & \mathbf{C}^{(2)} & \ddots & & & \vdots \\ \vdots & \ddots & \mathbf{C}^{(3)} & \ddots & & \vdots \\ \vdots & & \ddots & \ddots & \ddots & \vdots \\ \vdots & & & \ddots & \ddots & 0 \\ 0 & \cdots & \cdots & \cdots & 0 & \mathbf{C}^{(N_d)} \end{bmatrix} \quad (\text{A1})$$

Sparse matrices of diagonal $\mathbf{C}^{(k)}$, $\mathbf{K}^{(k)}$, $\mathbf{H}_{\text{int}}^{(k)}$, and $\mathbf{H}_{\text{ext}}^{(k)}$ are FE matrices for each substructure, which are defined by classical Lagrange linear finite-element basis functions $(\Psi_j^{(k)})_{1 \leq j \leq N^{(k)}}$:

$$\mathbf{C}^{(k)} = \left(\int_{\Omega^{(k)}} e c \Psi_i^{(k)} \Psi_j^{(k)} d\Omega \right)_{\substack{1 \leq i \leq N^{(k)} \\ 1 \leq j \leq N^{(k)}}} \quad (\text{A2})$$

$$\mathbf{K}^{(k)} = \left(\int_{\Omega^{(k)}} e \lambda \vec{\nabla} \Psi_i^{(k)} \cdot \vec{\nabla} \Psi_j^{(k)} d\Omega \right)_{\substack{1 \leq i \leq N^{(k)} \\ 1 \leq j \leq N^{(k)}}} \quad (\text{A3})$$

$$\mathbf{H}_{\text{int}}^{(k)} = \left(\int_{\Omega_{\text{int}}^{(k,e)}} h_{\text{int}} \Psi_i^{(k)} \Psi_j^{(k)} d\Omega \right)_{\substack{1 \leq i \leq N^{(k)} \\ 1 \leq j \leq N^{(k)}}} \quad (\text{A4})$$

$$\mathbf{H}_{\text{ext}}^{(k)} = \left(\int_{\Omega_{\text{ext}}^{(k)}} h_{\text{ext}} \Psi_i^{(k)} \Psi_j^{(k)} d\Omega \right)_{\substack{1 \leq i \leq N^{(k)} \\ 1 \leq j \leq N^{(k)}}} \quad (\text{A5})$$

The matrix of coupling \mathbf{J} is expressed as follows:

$$\mathbf{J} = \begin{bmatrix} 0 & \mathbf{J}_{1,2} & \mathbf{J}_{1,3} & \cdots & \cdots & \mathbf{J}_{1,N_d} \\ \mathbf{J}_{2,1} & 0 & \mathbf{J}_{2,3} & & & \vdots \\ \mathbf{J}_{3,1} & \mathbf{J}_{3,2} & 0 & \ddots & & \vdots \\ \vdots & & \ddots & \ddots & \ddots & \vdots \\ \vdots & & & \ddots & \ddots & \mathbf{J}_{N_d-1,N_d} \\ \mathbf{J}_{N_d,1} & \cdots & \cdots & \cdots & \mathbf{J}_{N_d,N_d-1} & 0 \end{bmatrix} \quad (\text{A6})$$

where each block corresponds to the finite-element matrices:

$$\mathbf{J}_{k_1,k_2} = \left(\int_{\Gamma_{\text{St}}^{(l)}} \frac{e}{R_{TC}} \left[\Psi_i^{(k)} \right]^{(l)} \left[\Psi_j^{(k)} \right]^{(l)} d\Gamma \right)_{\substack{1 \leq i \leq N^{(k)} \\ 1 \leq j \leq N^{(k)}}} \quad (\text{A7})$$

Vectors have the same construction methodology:

$$\mathbf{T} = \begin{bmatrix} \mathbf{T}^{(1)} \\ \mathbf{T}^{(2)} \\ \mathbf{T}^{(3)} \\ \vdots \\ \mathbf{T}^{(N_d)} \end{bmatrix} \quad (\text{A8})$$

$$\mathbf{T}^{(k)} = \left(T_i^{(k)} \right)_{1 \leq i \leq N^{(k)}} \quad (\text{A9})$$

Concerning the indoor temperatures, matrix \mathbf{U}_{cpl} is constructed by blocks with N_d submatrices of dimension $[N^{(k)} \times N_e]$:

$$\mathbf{U}_{\text{cpl}} = \begin{bmatrix} \mathbf{U}_{\text{cpl}}^{(1)} \\ \mathbf{U}_{\text{cpl}}^{(2)} \\ \mathbf{U}_{\text{cpl}}^{(3)} \\ \vdots \\ \mathbf{U}_{\text{cpl}}^{(N_d)} \end{bmatrix} \quad (\text{A10})$$

$$\mathbf{U}^{(k)} = \left(\int_{\Omega_{\text{int}}^{(k,e)}} h_{\text{int}} \Psi_i^{(k)} \Psi_j^{(k)} \right)_{\substack{1 \leq i \leq N^{(k)} \\ 1 \leq j \leq N^{(k)}}} \quad (\text{A11})$$

Also, $T_{\text{int}}^{(e)}$ is the temperature of an enclosure e defined in Equation (1). \mathbf{T}_{int} is expressed as follows:

$$\mathbf{T}_{\text{int}} = \begin{bmatrix} T_{\text{int}}^{(1)} \\ T_{\text{int}}^{(2)} \\ T_{\text{int}}^{(3)} \\ \vdots \\ T_{\text{int}}^{(N_e)} \end{bmatrix} \quad (\text{A12})$$

Finally, the vector of external stress \mathbf{U}_0 is heat flux losses by convection:

$$\mathbf{U}_0 = \begin{bmatrix} \mathbf{U}_0^{(1)} \\ \mathbf{U}_0^{(2)} \\ \mathbf{U}_0^{(3)} \\ \vdots \\ \mathbf{U}_0^{(N_d)} \end{bmatrix} \quad (\text{A13})$$

and in an elementary form:

$$\mathbf{U}_0^{(k)} = \left(\int_{\Omega_{\text{ext}}^{(k)}} h_{\text{ext}} \Psi_i^{(k)} T_{\text{ext}} d\Omega \right)_{1 \leq i \leq N^{(k)}} \quad (\text{A14})$$

APPENDIX B: MATRICES CONSTRUCTION OF A REDUCED PROBLEM

The reduced problem is constructed from matrices of the detailed problem and the couple of eigenvector $\widehat{\mathbf{V}}$ and vector of excitation states $\widehat{\mathbf{X}}$:

$$\widehat{\mathbf{V}} = \begin{bmatrix} \widetilde{\mathbf{V}}^{(1)} & 0 & \dots & \dots & \dots & 0 \\ 0 & \widetilde{\mathbf{V}}^{(2)} & \ddots & & & \vdots \\ \vdots & \ddots & \widetilde{\mathbf{V}}^{(3)} & \ddots & & \vdots \\ \vdots & & \ddots & \ddots & \ddots & \vdots \\ \vdots & & & \ddots & \ddots & 0 \\ 0 & \dots & \dots & \dots & 0 & \widetilde{\mathbf{V}}^{(N_d)} \end{bmatrix} \quad (\text{B1})$$

where each $\widetilde{\mathbf{V}}^{(k)}$ gathers the eigenvectors $\widetilde{\mathbf{V}}_i^{(k)}$ of a substructure (k) and could be defined by

$$\widetilde{\mathbf{V}}^{(k)} = \left[\widetilde{\mathbf{V}}_1^{(k)} \quad \widetilde{\mathbf{V}}_2^{(k)} \quad \widetilde{\mathbf{V}}_3^{(k)} \quad \dots \quad \widetilde{\mathbf{V}}_{\widetilde{N}^{(k)}}^{(k)} \right] \quad (\text{B2})$$

The vector of excitation states $\widehat{\mathbf{X}}$ is written as follows:

$$\widehat{\mathbf{X}} = \begin{bmatrix} \widetilde{\mathbf{X}}^{(1)} \\ \widetilde{\mathbf{X}}^{(2)} \\ \widetilde{\mathbf{X}}^{(3)} \\ \vdots \\ \widetilde{\mathbf{X}}^{(N_d)} \end{bmatrix} \quad (\text{B3})$$

APPENDIX C: WEAK FORMULATION OF BRANCH BASIS FOR A SHELL MODEL

The variational formulation is obtained in three steps:

- (16a) is multiplied by a test function $f \in H_1(\Omega)$ and integrated over $\Omega^{(k)}$:

$$\forall f \in H_1(\Omega), \int_{\Omega^{(k)}} e_0 \operatorname{div} \left(\lambda_0 \vec{\nabla} V_i^{(k)} \right) f^{(k)} d\Omega = \int_{\Omega^{(k)}} z_i^{(k)} \left(e_0 c_0 V_i^{(k)} + \delta_{(\Gamma_{st(i)}^{(k)})} e_0 \zeta V_i^{(k)} \right) f^{(k)} d\Omega. \quad (\text{C1})$$

- In Equation (C1), Green–Ostrogradsky formula is applied on the first member and Equation (17) for the second member:

$$\begin{aligned} \forall f \in H_1(\Omega), & - \int_{\Omega^{(k)}} e_0 \lambda_0 \vec{\nabla} f^{(k)} \cdot \vec{\nabla} V_i^{(k)} d\Omega + \int_{\Gamma_{st(i)}^{(k)}} e_0 \lambda_0 f^{(k)} \vec{\nabla} V_i^{(k)} \cdot \vec{n}_{\Gamma_{st}^{(k)}} d\Gamma \\ & = z_i^{(k)} \left(\int_{\Omega^{(k)}} e_0 c_0 V_i^{(k)} f^{(k)} d\Omega + \int_{\Gamma_{st(i)}^{(k)}} e_0 \zeta V_i^{(k)} f^{(k)} d\Gamma \right). \end{aligned} \quad (\text{C2})$$

- Equation (C2) could be simplified with Equation (16b)

$$\begin{aligned} \forall f \in H_1(\Omega), & - \int_{\Omega^{(k)}} e_0 \lambda_0 \vec{\nabla} f^{(k)} \cdot \vec{\nabla} V_i^{(k)} d\Omega - \int_{\Gamma_{st(e)}^{(k)}} z_i^{(k)} e_0 \zeta V_i^{(k)} f^{(k)} d\Gamma \\ & = z_i^{(k)} \left(\int_{\Omega^{(k)}} e_0 c_0 V_i^{(k)} f^{(k)} d\Omega + \int_{\Gamma_{st(i)}^{(k)}} e_0 \zeta V_i^{(k)} f^{(k)} d\Gamma \right). \end{aligned} \quad (C3)$$

The weak formulation for a shell model of Equation (16), after a simplification by Equation (6), is written in a compact form as follows:

$$\forall f \in H_1(\Omega), \int_{\Omega^{(k)}} e_0 \lambda_0 \vec{\nabla} f^{(k)} \cdot \vec{\nabla} V_i^{(k)} d\Omega = -z_i^{(k)} \left(\int_{\Omega^{(k)}} e_0 c_0 V_i^{(k)} f^{(k)} d\Omega + \int_{\Gamma_{st}^{(k)}} e_0 \zeta V_i^{(k)} f^{(k)} d\Gamma \right). \quad (C4)$$